Int. J. Electrochem. Sci., 12 **(2017)** 12074 – 12083, doi: 10.20964/2017.12.300

International Journal of
ELECTROCHEMICAL
SCIENCE
www.electrochemsci.org

Effect of Nitrogen Content on the Corrosion Resistance of Zr-Ni-Al-Si Thin Film Metallic Glass

Chia-Lin Li[1], *Ching-Yen Chung*[2], *Bih-Show Lou*[3,4], *Jyh-Wei Lee*[2, 5,6,*], *Jinn P. Chu*[1,7]

[1] Graduate Institute of Applied Science and Technology, National Taiwan University of Science and Technology, Taipei, Taiwan
[2] Department of Materials Engineering, Ming Chi University of Technology, New Taipei City, Taiwan
[3] Chemistry Division, Center of General Education, Chang Gung University, Taoyuan, Taiwan
[4] Department of Nuclear Medicine and Molecular Imaging Center, Chang Gung Memorial Hospital, Taoyuan, Taiwan
[5] Center for Thin Film Technologies and Applications, Ming Chi University of Technology, New Taipei City, Taiwan
[6] College of Engineering, Chang Gung University, Taoyuan, Taiwan
[7] Department of Materials Science and Engineering, National Taiwan University of Science and Technology, Taipei, Taiwan
[*]E-mail: jefflee@mail.mcut.edu.tw

Received: 4 July 2017 / *Accepted:* 20 October 2017 / *Published:* 12 November 2017

Nitrogen-free and nitrogen-doped Zr-Ni-Al-Si thin film metallic glasses (TFMGs) were prepared through a plasma emission monitoring (PEM) control process in a co-sputtering system. The corrosion behaviors of these TFMGs coated onto AISI 420 stainless steel substrates in 3.5 wt. % aqueous sodium chloride were studied using electrochemical impedance spectroscopy and equivalent circuit simulation. Nitrogen contents of 11.1 and 15.4 at. % were obtained for TFMGs fabricated under 30 and 70% Zr target poisoning rates, respectively. The amorphous and nitrogen-free TFMG provided the highest corrosion impedance after one hour of immersion in 3.5 wt.% aqueous sodium chloride due to its featureless and dense microstructure. However, the corrosion impedance values of this nitrogen-free TFMG decreased rapidly after immersion for 12 and 24 hours, which could be attributed to its poor adhesion to the AISI 420 stainless steel substrate. Meanwhile, the 15.4 at. % N-doped TFMG showed a stable and good corrosion resistance after immersion for 1 to 24 hours due to its dense nanocomposite microstructure consisting of ZrN nanograins embedded in an amorphous matrix. The lowest corrosion impedance values were found for the TFMG containing 11.1 at. % nitrogen, and this finding can be attributed to the columnar microstructure of this TFMG, which provides a shortcut for the corrosive electrolyte to penetrate through the boundaries to the AISI 420 stainless steel substrate.

Keywords: Zr-Ni-Al-Si thin film metallic glass, plasma emission monitoring, target poisoning, corrosion test, electrochemical impedance spectroscopy

1. INTRODUCTION

Recently, research into amorphous bulk metallic glasses (BMGs) has included innovative work toward the development of new materials because of the unique strength, good corrosion and wear resistance of these amorphous materials [1]. Since brittleness restricts the applications of BMGs, an alternative amorphous counterpart, the so-called thin film metallic glass (TFMG), has been developed and considered ~~as~~ a potential solution to overcoming this problem [1]. In the literature, physical vapor deposition (PVD) methods [1-4], such as sputtering, have been employed to fabricate TFMGs. These sputtered TFMGs provide ~~a~~ great enhancement of the fatigue life of a 316L stainless steel bar [4, 5]. Satisfactory Young's modulus and hardness after proper thermal annealing can be obtained [6, 7]. Better mechanical properties were observed after doping ~~into~~ the Zr-Ni-Al-Si TFMGs with nitrogen [8]. We find that the added element and its concentration have a notable influence on the characteristics of TFMGs. For instance, the addition of nitrogen and boron atoms can improve the hardness (up to 16.2 GPa) and toughness of Zr-based TFMGs due to the denser atomic packing and reduced free volume [9]. Furthermore, the addition of other elements, such as Si, W, and Fe, to generate Zr–Ti–B–Si, Zr–W–Ti and Fe–Zr–Ti TFMGs, respectively, has been shown to affect the corrosion resistance of amorphous coatings [10-12].

The corrosion resistance of BMGs has been reported to be superior to that of their crystalline counterparts because they lack obvious shortcuts or defects, such as grain boundaries and dislocations ~~for~~ through which the corrosive electrolyte ~~to~~ could attack [13, 14]. In addition, the corrosion properties and related mechanisms of Zr-Cu-Ni-Al TFMG have also been studied[15]. Feature corrosion patterns, such as radial wrinkles and river-flow, were observed adjacent to the corrosion pits. However, the localized Cu-rich nanoscale region became the location of attack, leading to a lower corrosion resistance, which was confirmed by the appearance of Cu-rich corrosion products inside the pit. Similar appearances of Cu-rich oxide corrosion products have also been observed in BMGs [16, 17]. Consequently, Cu-free BMGs [16, 18] have been developed ~~for~~ to enhance corrosion resistance. In our previous work, we developed Zr-Ni-Al-Si TFMGs in the absence of Cu and introduced different concentrations of nitrogen [8]. The changes in the corresponding microstructures and mechanical properties with respect to the nitrogen content of these TFMGs were fully explored [8]. A nanocomposite microstructure consisting of ZrN nanograins embedded in the amorphous matrix has become a promising method to further enhance the mechanical properties of TFMGs. However, the effects of nitrogen content and the microstructure on the corrosion resistance of such Zr-Ni-Al-Si TFMGs have not yet been elucidated. In this study, as a continuation of our previous work, the corrosion resistances of the nitrogen-free and nitrogen-containing Zr-Ni-Al-Si TFMGs were explored. The possible mechanism for the corrosion behavior of Zr-Ni-Al-Si and Zr-Ni-Al-Si-N TFMGs is discussed.

2. EXPERIMENTAL PROCEDURES

Three Zr-Ni-Al-Si thin film metallic glasses were co-sputtered on p-type (100) Si wafers and hardened AISI 420 stainless steel substrates using a carousel type of radio-frequency (RF) and pulsed direct-current (DC) magnetron sputtering. The manufacturing details of these films have been reported in our previous work [8]. To precisely control ~~of~~ the nitrogen dopant concentrations in the amorphous thin film, a plasma emission monitoring system (PEM, PLASUS EMICON, Germany) was used to monitor the plasma emission spectrum and to control the flow rate of the reactive N_2 gas by a piezoelectric valve [8]. Prior to deposition, the intensity of Zr at 389 nm in the plasma [19] versus the N_2 flow rate was monitored by PEM to determine the poisoning rate of Zr target. Three poisoning rates, 0%, 30% and 70%, were selected to fabricate three TFMGs that were designated ZN-0, ZN-3, and ZN-7, respectively.

The corrosion resistance of each film deposited on the AISI 420 stainless steel substrates was evaluated by electrochemical impedance spectroscopy (EIS), which was conducted in 3.5 wt. % aqueous sodium chloride using a potentiostat (VersaSTAT 4, Princeton Applied Research, USA) equipped with an internal frequency response analyzer. A standard cell with three electrodes was used. The auxiliary and reference electrodes were platinum and saturated calomel, respectively. The EIS spectra were acquired in the frequency range of 0.01 Hz to 100 kHz. An AC potential amplitude of 10 mV was applied to the electrode at its corrosion potential. Impedance data at the corrosion potential were collected after 1, 12, and 24 hours of immersion time. The data were interpreted based on an equivalent circuit by fitting with Z-view software. The surface morphologies of the corroded films after 24 hr of immersion were further investigated by a scanning electron microscope (SEM).

3. RESULTS AND DISCUSSION

3.1 Chemical composition and phase characterization

According to our previous study [8], the chemical compositions of the three TFMGs are $Zr_{62.5}Ni_{18.4}Al_{7.1}Si_{9.7}O_{2.4}$ (ZN-0), $Zr_{53.9}Ni_{17.6}Al_5Si_{8.3}O_4N_{11.1}$ (ZN-3) and $Zr_{48.9}Ni_{19.5}Al_{3.7}Si_{7.3}O_{5.1}N_{15.4}$ (ZN-7. The nitrogen content increased suddenly from 0 to 11.1 at.% and then increased gradually up to 15.4 at.% as the target poisoning rate increased from 0 to 30% and then up to 70%. The chemical compositions of Zr, Al and Si decreased with increasing target poisoning rate. Fig. 1 shows the X-ray diffraction patterns of the three TFMGs [8]. Only a broad hump is observed in the range of 33°- 43° for ZN-0, indicating an amorphous structure. In contrast, the diffraction peaks of ZN-3 and ZN-7 became sharper when the target poisoning rate and nitrogen content increased because of the formation of nanocrystalline ZrN phases. The absence of AlN and Si_3N_4 peaks indicates that the nitridation process presumably occurs only on Zr. The average grain sizes of ZN-3 and ZN-7 were calculated ~~by~~ according to the Scherrer formula [20] to be 2.4 and 3.3 nm, respectively. The formation of these fine nanograins in the nitrogen- containing TFMGs is attributed to the grain growth suppression by the amorphous matrix. In our previous work [8], the high-resolution TEM bright field image and corresponding electron diffraction patterns revealed that no crystalline phases or nanograins are present in ZN-0, while the ZrN nanograins embedded in the amorphous matrix are found in the nitrogen-doped TFMGs. The cross-sectional morphologies of the three TFMGs are shown in Fig. 2 [8].

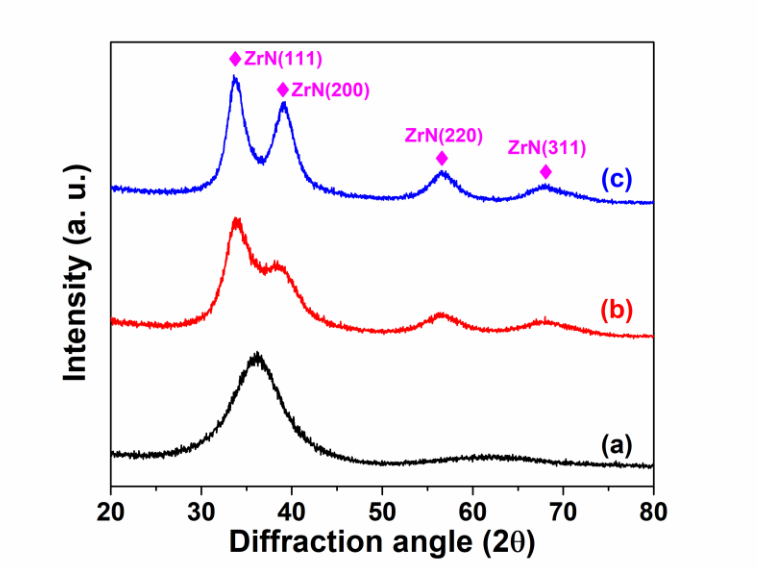

Figure 1. X-ray diffraction patterns of (a) ZN-0, (b) ZN-3, and (c) ZN-7 TFMGs

ZN-0 TFMG has a featureless microstructure. In contrast, a typical columnar structure is observed for ZN-3. A very fine and dense microstructure can be seen for ZN-7 in Fig. 2(c). It seems that the columnar structure becomes finer and denser as the nitrogen content increases due to the formation of fine nanograins. Furthermore, the film thickness values of ZN-0, ZN-3, and ZN-7 are 1100, 760 and 586 nm, respectively, which shows a decreasing tendency with an increasing target poisoning rate [8].

3.2 Corrosion resistance evaluation

The EIS Bode plot of each film is shown in Fig. 3, which illustrates the relationship between the impedance, phase angle and frequency. For the ZN-0 and ZN-7 TFMGs, the Bode plot data depict one time constant after different immersion time intervals in Figs. 3(a) and (c). However, as expected, two time constants are observed for ZN-3 and this is accompanied by a continuous decrease in the absolute values of the impedance, which becomes more obvious at the lower frequencies (Fig. 3(b)). Almost no obvious differences are found in the EIS spectra ZN-7 TFMG after longer immersion times, as shown in Fig. 3(c), indicating that a rather stable and good corrosion resistance is achieved. Two kinds of equivalent circuit modeling are proposed based on the EIS data and microstructure of the films. The equivalent circuit for each film is also depicted in Fig. 3 and illustrates the electrochemical cell of the solution/TFMG/SUS420 substrate assembly. RE and WE represent the reference electrode and working electrode, respectively. Rs is the solution resistance. C1 is the capacitance of the TFMG (ZN-3); CPE1 is the capacitance of the solution/substrate for ZN-3 and the capacitance of the solution/TFMG interfaces for ZN-0 and ZN-7 TFMGs. R_{pore} is the resistance of the TFMG resulting from the defects. R_{ct} is the charge transfer resistance of the TFMG/substrate interface for ZN-3. The fitting errors of each part ~~for~~ of the equivalent circuit models are smaller than 10%. The fitting values for the various parameters after immersion for different time intervals are listed in Table 1.

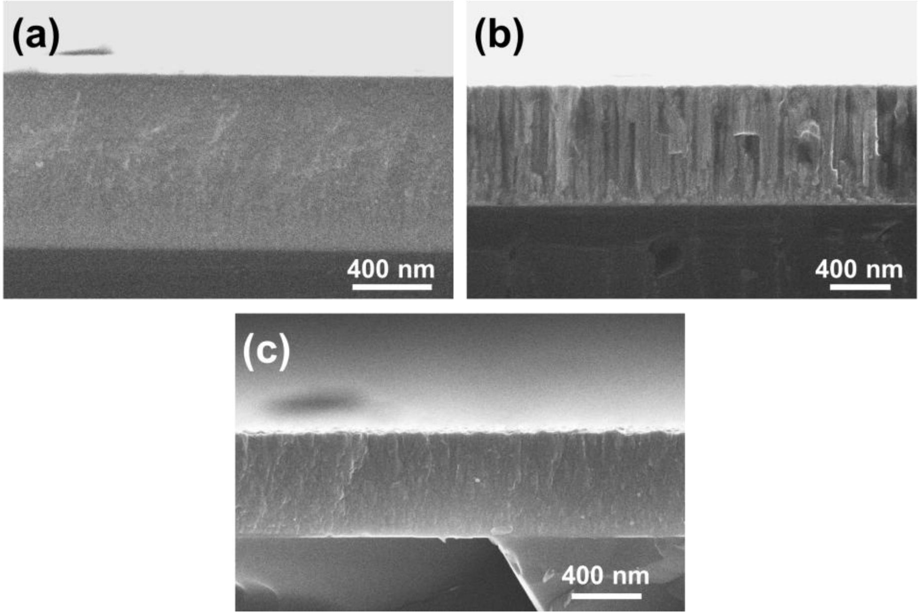

Figure 2. Cross-sectional SEM images of (a) ZN-0, (b) ZN-3, and (c) ZN-7 TFMGs

In general, the corrosion process starts from the penetration of the electrolyte through the surface defects, such as columnar structure boundaries or pinholes ~~to~~ in the electrolyte/TFMG interface, which dominates the corrosion resistance of the TFMG/substrate assembly [21]. The highest resistance (R_{pore}= 477.4 kΩ-cm^2) was observed for the thickest amorphous ZN-0 TFMG, which has a featureless microstructure, after 1 hr immersion, and then, the R_{pore} value decreases drastically to 97.8 kΩ-cm^2 as the immersion time increased to 24 hr. We suggest that this degradation may be caused by its poor adhesion onto the SUS420 substrate [8]. The thinnest ZN-7 TFMG was found to be more stable, and less degradation of film resistance was observed; resistance values of 140.3 to 102.1 kΩ-cm^2 were found ~~as~~ after the sample ~~is~~ had been exposed to the corrosive electrolyte for 1 hr and 12 hr, respectively. Moreover, a higher film resistance of 126.6 kΩ-cm^2 ~~is~~ was further observed due to the plugging effect by corrosion products [22] and the nanocomposite microstructure [8]. We suggest that a much longer immersion time is required for the NaCl electrolyte to penetrate through the large amount of nanosized grain boundaries in the dense and compact structure to reach the substrate. A similar result was also reported in a corrosion study of a nanocrystalline copper thin film [23], which attributed the relatively low corrosion to the increments of boundaries per unit area. Based on the R_{ct} values of ZN-3 TFMG for different immersion time intervals, the charge transfer resistance of the TFMG/substrate interface decreases drastically with increasing immersion time, which is mainly caused by its coarse columnar structure, as shown in Fig. 2(b).

According to our previous study [8], the coarse columnar structure of ZN-3 was produced due to the relatively high deposition rate and low target poisoning effect.

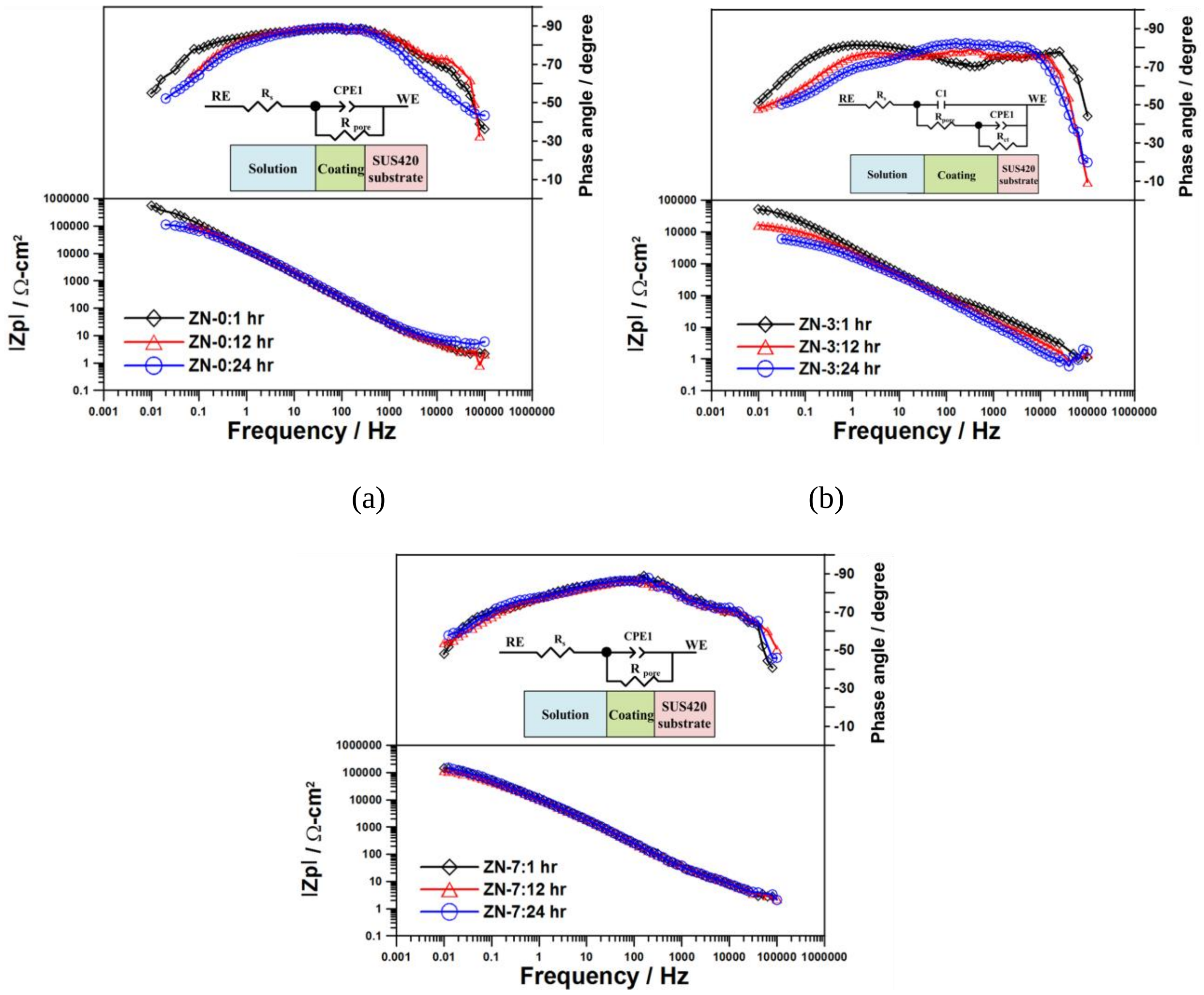

(a) (b)

(c)

Figure 3. Bode plots and equivalent circuits of the EIS data of (a) ZN-0, (b) ZN-3 and (c) ZN-7 exposed to 3.5 wt.% NaCl solution for different immersion time intervals.

Table 1. Electrochemical parameters obtained from equivalent circuit simulations for ZN-0, ZN-3, and ZN-7 in 3.5 wt.% NaCl solution.

Sample	Target poisoning rate (%)	Immersion Time (hr)	R_s (Ω-cm^2)	C1 (μF/cm^2)	R_{pore} (kΩ-cm^2)	CPE1 (μF/cm^2)		R_{ct} (kΩ-cm^2)
						CPE-T	n (0-1)	
ZN-0	0	1	1.858	--	477.4	10.68	0.896	--
		12	1.755	--	140.2	10.96	0.887	--
		24	4.342	--	97.8	11.49	0.883	--
ZN-3	30	1	0.896	2.38	0.025	57.03	0.767	57.2
		12	1.125	4.49	0.012	88.16	0.689	15.4
		24	0.619	7.71	0.006	109.73	0.642	6.1
ZN-7	70	1	1.823	--	140.3	18.08	0.801	--
		12	1.747	--	102.1	18.51	0.798	--
		24	2.094	--	126.6	17.16	0.811	--

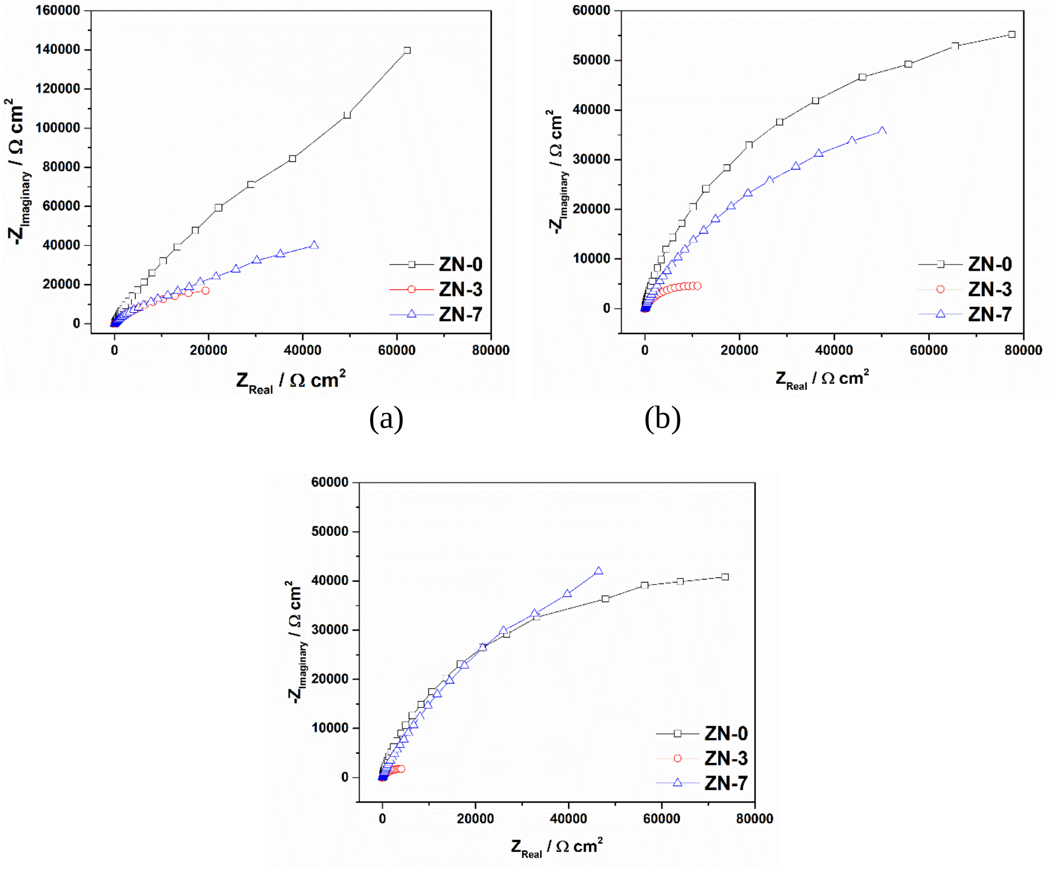

(a) (b)

(c)

Figure 4. Nyquist plots of ZN-0, ZN-3 and ZN-7 in 3.5 wt.% NaCl solution for (a) 1 hr, (b) 12 hr and (c) 24 hr immersion time intervals

EIS measurements of all samples, illustrated as Nyquist plots that include the real and imaginary parts of the impedance as a function of the applied frequency perturbation, are shown in Fig. 4. We can see that each plot can be presented in a typical semicircle. In general, semicircles with larger diameters represent better corrosion resistance. Consequently, the ZN-0 sample, which has the semicircle with the largest diameter, clearly exhibits the highest corrosion resistance after 1 and 12 hr of immersion. However, the semicircle with the smallest diameter can be observed in the ZN-3 sample for all immersion time intervals. As seen in Figs. 4(a) to (c), the decrease in the diameters of the semicircles with increasing immersion times corresponds to the decreasing R_{pore} values from 0.025 to 0.006 kΩ-cm^2 ~~of~~ for ZN-3, which is the smallest value among the tested films. This finding suggests that the ZN-3 sample shows the worst anti-corrosion property owing to its coarse columnar structure. Many studies evaluating the corrosion properties of thin films have noted that the voids among columnar grains become the diffusion paths for the penetration of corrosive electrolytes and thereby lead to poor anti-corrosion abilities [21, 24, 25].

In addition, the corroded surface morphologies of ZN-0, ZN-3 and ZN-7 films after 24 hr of immersion are presented in Figs. 5-7, respectively. Top-view SEM images of a corrosion pit filled with iron oxide particles and a severe pitting corrosion of underlying AISI420 stainless steel due to ZN-0 film rupture after 24 hr of immersion are shown in Fig. 5 (a) and (b), respectively. Obviously, many isolated and deep disc-like pits on the AISI 420 substrate are produced due to the corrosive electrolyte attacking the local minor defects of the amorphous and featureless ZN-0 film during the corrosion stage. Apparently, these deep disc-like pits were formed after the protective ZN-0 film spalled away locally due to its poor adhesion. Such corrosion behavior, for either disc-like pits or iron oxide particles, was also observed on the surface of corroded amorphous iron-based TFMG [26] as well as in a study of typical TiN thin film corrosion [24]. Figs. 6 (a) and (b) depict the corroded surface ~~on~~ of the ZN-3 film. The large particles of corrosion products from the AISI420 steel substrate (indicated by an arrow), corrosion pits, and cracked and spalled ZN-3 film are shown in Fig. 6(a). The surface morphology of a corrosion pit at higher magnification is illustrated in Fig. 6(b) and shows the severely corroded AISI420 steel (S) and swelled film (C) due to the extrusion of iron oxide products. Large amounts of oxide corrosive products and undercutting pits are noticeable in the ZN-3 sample, indicating that this film has the worst anti-corrosion nature, which results in the lowest R_{pore} values.

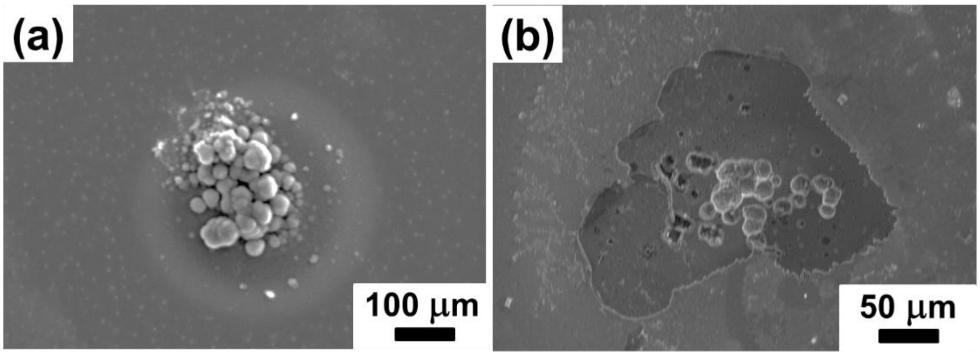

Figure 5. Top-view SEM images of the corroded surface ~~on~~ of the ZN-0 film including (a) a corrosion pit filled with iron oxide particles and (b) severe pitting corrosion of underlying AISI420 stainless steel

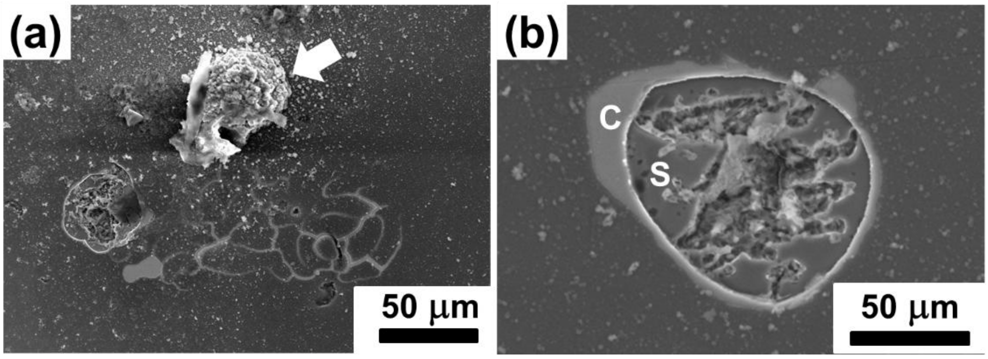

Figure 6. Top-view SEM images of the corroded surface of the ~~on~~ ZN-3 film, including (a) large particles of corrosion product from the AISI420 steel substrate (indicated by an arrow), corrosion pits, and cracked and spalled ZN-3 film and (b) severely corroded AISI420 steel (S) and swelled film (C)

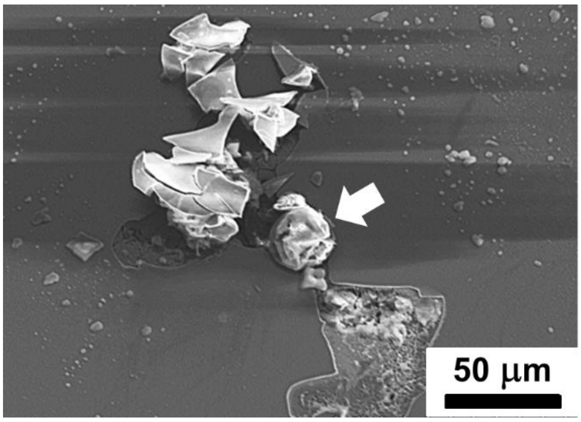

Figure 7. Top-view SEM image of a corroded surface on ZN-7

A top-view SEM image of the corroded surface of the ZN-7 is shown in Fig. 7. It is important to note that disc-like pits such as the one shown in Fig. 5(b) are not observed in the ZN-7 samples, suggesting ~~a~~ more stable degradation ~~of~~ and greater corrosion resistance. Spallation of films by the extrusion of iron oxide products ~~of~~ from the SUS420 substrate after the electrolyte penetrates the film (indicated by an arrow) can be seen on the surface of the ZN-7 sample, as displayed in Fig. 7.

Based on the corrosion morphologies observed in Figs. 5-7, we can conclude that a featureless amorphous microstructure and a dense nanocomposite microstructure can effectively retard the attack of corrosive electrolyte for a short time period. In contrast, a coarse columnar microstructure will provide shortcuts for the electrolyte to attack the substrate and therefore exhibits a poor corrosion resistance. Finally, the adhesion of the thin film onto the AISI 420 stainless steel substrate is a very important factor because spallation of the thin film from the underlying substrate will quickly ruin the corrosion protection.

4. CONCLUSIONS

In this work, we studied the effect of nitrogen concentration, ranging from 0 to 15.4 at. %, on the corrosion resistance of Zr-Ni-Al-Si TFMGs. The nitrogen-free TFMG (ZN-0) showed the highest corrosion resistance (R_{pore} = 477.4 kΩ-cm^2) at the initial corrosion stage of 1 hr due to its amorphous and featureless microstructure. Because of its coarse columnar structure, the 11.1 at.% nitrogen-containing TFMG (ZN-3) exhibited the worst anti-corrosion ability and the lowest R_{pore} value (0.025 kΩ-cm^2) for all immersion time intervals. The ZN-7 TFMG (15.4 at. % N) presents a stable and good corrosion resistance after 24 hr of immersion due to its nanocomposite microstructure consisting of ZrN nanograins embedded in an amorphous matrix. Finally, the microstructure and film adhesion play important roles on the corrosion resistance brought by the nitrogen-doped Zr-Ni-Al-Si TFMGs.

ACKNOWLEDGEMENTS
The authors gratefully acknowledge the financial support of the Ministry of Science and Technology, Taiwan, through contract Nos. MOST 100-2221-E-131-008-MY3, MOST 101-2221- E-011-048- MY3 and MOST 105-2218-E-131-001.

References

1. J.P. Chu, J. Jang, J. Huang, H. Chou, Y. Yang, J. Ye, Y. Wang, J. Lee, F. Liu, P. Liaw, *Thin Solid Films*, 520 (2012) 5097.
2. S. Hata, R. Yamauchi, J. Sakurai, A. Shimokohbe, *Jpn. J. Appl. Phys*., 45 (2006) 2708.
3. C.-J. Lin, F. Spaepen, *Acta Metall*., 34 (1986) 1367.
4. C. Chiang, J. Chu, F. Liu, P. Liaw, R. Buchanan, *Appl. Phys. Lett*., 88 (2006) 131902.
5. J.P. Chu, C.-M. Lee, R. Huang, P. Liaw, *Surf. Coat. Technol*., 205 (2011) 4030.
6. J. Chu, C. Liu, T. Mahalingam, S. Wang, M. O'Keefe, B. Johnson, C. Kuo, *Phys. Rev*. B, 69 (2004) 113410.
7. J. Chu, JOM, 61 (2009) 72.
8. C.-Y. Chuang, J.-W. Lee, C.-L. Li, J.P. Chu, *Surf. Coat. Technol.*, 215 (2013) 312.
9. T.-P. Hsiao, Y.-C. Yang, J.-W. Lee, C.-L. Li, J.P. Chu, *Surf. Coat. Technol.*, 237 (2013) 276.
10. J.-C. Chang, J.-W. Lee, B.-S. Lou, C.-L. Li, J.P. Chu, *Thin Solid Films*, 584 (2015) 253.
11. L.-T. Chen, J.-W. Lee, Y.-C. Yang, B.-S. Lou, C.-L. Li, J.P. Chu, *Surf. Coat. Technol*., 260 (2014) 46.
12. Y.-L. Deng, J.-W. Lee, B.-S. Lou, J.-G. Duh, J.P. Chu, J.S.-C. Jang, *Surf. Coat. Technol*., 259, Part B (2014) 115.
13. W. Peter, R. Buchanan, C. Liu, P. Liaw, M. Morrison, J. Horton, C. Carmichael, J. Wright, *Intermetallics*, 10 (2002) 1157.
14. J.R. Scully, A. Gebert, J.H. Payer, *J. Mater. Res*., 22 (2007) 302.
15. C.-Y. Chuang, Y.-C. Liao, J.-W. Lee, C.-L. Li, J.P. Chu, J.-G. Duh, *Thin Solid Films*, 529 (2013) 338.
16. Y.H. Li, W. Zhang, C. Dong, J.B. Qiang, M. Fukuhara, A. Makino, A. Inoue, *Mater. Sci. Eng*. A, 528 (2011) 8551.
17. W. Zhou, W.P. Weng, J.X. Hou, *J. Mater. Sci. Technol*., 32 (2016) 349.
18. B. Guan, X. Shi, Z. Dan, G. Xie, M. Niinomi, F. Qin, *Intermetallics*, 72 (2016) 69.
19. K. Salmenoja, A. Korhonen, *Vacuum*, 36 (1986) 33.
20. A. Patterson, *Phys. Rev.*, 56 (1939) 978.
21. C. Liu, Q. Bi, A. Leyland, A. Matthews, *Corros. Sci*., 45 (2003) 1257.
22. C. Liu, A. Leyland, S. Lyon, A. Matthews, *Surf. Coat. Technol*., 76 (1995) 623.
23. E.M. Pinto, A.S. Ramos, M.T. Vieira, C.M. Brett, *Corros. Sci*., 52 (2010) 3891.
24. Q. Wan, H. Ding, M. Yousaf, Y. Chen, H. Liu, L. Hu, B. Yang, *Thin Solid Films*, 616 (2016) 601.
25. C. Liu, Q. Bi, A. Matthews, *Corros. Sci*., 43 (2001) 1953.
26. Z. Li, C. Zhang, L. Liu, *J. Alloys Compd*., 650 (2015) 127.